Tellus (1993), *45A*, 28–43

Stagnation points and bifurcation in 3-D mountain airflow

By RONALD B. SMITH, *Department of Geology and Geophysics, Yale University, New Haven, CT, USA*
and SIGBJØRN GRØNÅS, *Institute of Geophysics, University of Bergen, Bergen, Norway*

(Manuscript received 8 January 1992; in final form 22 June 1992)

ABSTRACT

The effect of non-linearity on the formation of mountain-wave induced stagnation points is examined using the scaling laws for ideal hydrostatic flow and a series of runs with decelerating winds in a numerical model. In the limit of small deceleration rate, (i.e., near steady state) runs with a variety of mountain heights and widths give similar results; i.e., the speed extrema values in the 3-D wave fields collapse onto "universal curves". For a Gaussian hill with circular contours, stagnation first occurs at a point above the lee slope. This result contradicts the result of linear theory that stagnation begins on the windward slope. The critical value of $\hat{h}$ for stagnation above a Gaussian hill is $\hat{h}_{crit} = 1.1 \pm 0.1$. For a 3/2-power hill, the critical height is slightly higher, $\hat{h}_{crit} = 1.2 \pm 0.2$. These values are significantly larger than the value for a ridge ($\hat{h}_{crit} = 0.85$), due to dispersion of wave energy aloft. The application of Sheppard's rule and the vorticity near the stagnation point are discussed. As expected from linear theory, the presence of positive windshear suppresses stagnation aloft. With Richardson number = 20 for example, stagnation first begins at the ground at a value of $\hat{h} = 1.6 \pm 0.2$. When a stagnation point first forms aloft in the unsheared case, the flow field begins to evolve in the time domain and the scaling laws are violated. We interpret these events as a wave-breaking induced bifurcation which leads to stagnation on the windward slope and the formation of a wake.

1. Introduction

The formation of stagnation points in stratified air flow over a hill has been investigated by Smith (1989a) using linear theory. According to this theory, two preferred points for flow stagnation exist over a simple isolated hill; one at the lower boundary on the windward slope (point B) and one at a point in the fluid located some distance above the leeward slope (point A). For long ridges oriented perpendicularly to the flow, the tendency for stagnation at point A is far stronger than at B, while for hills with circular topographic contours, the two points are equally significant.

The significance of flow stagnation in stratified flow can be profound, at least in two-dimensional flow. Long (1955) suggested that regions aloft nearing stagnation (i.e., point A) would be associated with steeply sloping streamlines and incipient overturning, leading to turbulence. Huppert and Miles (1969) found the critical hill height to be $\hat{h} = h_0 N_0 / U_0 \approx 0.85$ for a simple ridge in 2-D flow. Clark and Peltier (1977) found that when this critical value of $\hat{h}$ is exceeded, a turbulent patch appears and the flow begins to change in time, eventually reaching a new "severe wind" steady state. In the new steady state, the wave breaking decouples the flow below from the flow above the breaking region, allowing the flow below to be well described by a local hydraulic theory (Smith, 1985).

The significance of flow stagnation in 3-D flows has received less attention. The two obvious possibilities are first, stagnation and wave overturning at A could trigger severe downslope flow as in 2-D. Second, stagnation at B could allow flow splitting; i.e., the left-right splitting of the low level center streamline so that the flow passes around instead of over the hill. This latter idea has been put forward in a number of contexts. (Sheppard, 1956; Drazin, 1961; Hunt and Snyder, 1980; Smolarkiewicz and Rotunno, 1990). These approaches have been recently reviewed by Smith (1989b). Other possibilities are equally probable. For example, wave over-turning aloft could trigger a bifurcation which, after some adjustment in the

time domain, could lead to a new steady state with low level flow splitting.

The formation of stagnation points may also be connected to the phenomenon of the mountain wake. The wake behind smooth low hills in stratified flow has been studied in the laboratory (Brighton, 1978; Castro et al., 1983; Castro, 1987; Hunt and Snyder, 1980) and in recent numerical simulations by Smolarkiewicz and Rotunno (1989a, hereafter SR89) and Crook et al. (1990). SR89 suggest that vorticity near the incipient lee side stagnation point (A) in steady flow may be a precursor of wake eddies that appear for higher mountains.

The purpose of this study is to investigate the effect of non-linearity on the formation of stagnation points in 3-D mountain waves.

1.1. Governing equations

The Boussinesq equations which govern stratified incompressible airflow are

$$\rho_0 \frac{\partial \boldsymbol{U}_H}{\partial t} + \rho_0 \boldsymbol{U} \cdot \nabla \boldsymbol{U}_H + \rho_0 f \boldsymbol{k} \times \boldsymbol{U}_H = -\nabla_H p - \nabla \cdot \boldsymbol{F}, \tag{1}$$

$$\rho_0 \frac{Dw}{Dt} = -p_z - b, \tag{2}$$

$$\nabla \cdot \boldsymbol{U} = 0, \tag{3}$$

$$\frac{\partial b}{\partial t} + \boldsymbol{U} \cdot \nabla b = -\nabla \cdot \boldsymbol{B}, \tag{4}$$

where ρ_0 = reference density, $b = \rho g$ = buoyancy, $\boldsymbol{F}_H$ = viscous or turbulent flux of horizontal momentum and, $\boldsymbol{B}$ = diffusive or turbulent flux of buoyancy.

For the present purposes we consider an idealized hydrostatic non-rotating "prototype" problem as the basis for our stagnation study (Smith, 1989b). The turbulent flux terms in eqs. (1–4) are dropped with the caution that under some conditions there may be no solution or no stable solution to the prototype problem with these terms absent. In such a case, the flux terms may have to be recalled for physical consistency.

The remaining terms in (1–4) can be non-dimensionalized using the following dimensional parameters: h_0 = maximum mountain height; U_0 = undisturbed flow speed; N_0 = undisturbed static stability; L = mountain width. Using a method of scaling derived from linear theory $U = U_0(z) + u$; $V = v$; $W = w$; $p = P_0(z) + p$; $b = b_0(z) + b$ where each lower case quantity is a function of x, y, and z and has a scale $u \sim U^* \equiv U_0 \hat{h}$; $v \sim V^* \equiv U_0 \hat{h}$; $w \sim W^* \equiv U_0^2 \hat{h}/LN_0$; $p \sim P^* \equiv \rho_0 N_0 U_0 h_0$; $b \sim b^* \equiv \rho_0 N_0^2 h_0$ where $\hat{h} = h_0 N_0 / U_0$.

Spatial derivatives have scales $\partial/\partial x \sim \partial/\partial y \sim (1/L)\,\partial/\partial z \sim 1/L_z$ where $L_z = U_0/N_0$.

Defining non-dimensional variables $\hat{u} = u/U^*$ etc. and $\hat{x} = x/L$, etc., and $\hat{z} = z/L_z$, the steady idealized version of eqs. (1–4) becomes

$$(1 + \hat{h}\hat{u})\,\hat{u}_{\hat{x}} + \hat{h}\hat{v}\hat{u}_{\hat{y}} = -\hat{p}_{\hat{x}}, \tag{5}$$

$$(1 + \hat{h}\hat{u})\,\hat{v}_{\hat{x}} + \hat{h}\hat{v}\hat{v}_{\hat{y}} = -\hat{p}_{\hat{y}}, \tag{6}$$

$$0 = -\hat{p}_{\hat{z}} - \hat{b}, \tag{7}$$

$$\hat{u}_{\hat{x}} + \hat{v}_{\hat{y}} + \hat{w}_{\hat{z}} = 0, \tag{8}$$

$$(1 + \hat{h}\hat{u})\,\hat{b}_{\hat{x}} + \hat{h}\hat{v}\hat{b}_{\hat{y}} + (1 + \hat{h}\hat{b}_{\hat{z}})\,\hat{w} = 0. \tag{9}$$

The lower boundary condition for the prototype problem

$$w(z = h) = (U_0 + u)\frac{\partial h}{\partial x} + v\frac{\partial h}{\partial y}, \tag{10}$$

with $h = h(x, y)$. In non-dimensional form, eq. (10) is

$$\hat{w}(\hat{z} = \hat{h}) = (1 + \hat{h}\hat{u})\,\hat{h}_{\hat{x}} + (\hat{h}\hat{v})\,\hat{h}_{\hat{y}}, \tag{11}$$

where $\hat{h} = h_0/L_z$.

A radiation condition is used as the upper boundary condition. As we consider only 3-D flows which naturally disperse and weaken aloft, it is sufficient to consider a linear radiation condition. As a radiation condition involves only phase line slope or the sign of the energy flux, it introduces no new control parameters or length scales.

The set of equations 5–9, 11 contains only one control parameter $\hat{h}$. Each non-linear term has $\hat{h}$ as a coefficient.

1.2. Scaling laws

Inspection of eqs. (5–9, 11) gives two scaling laws.

(i) Any combination of changes in U_0, N_0, h_0, z which maintain the values of $\hat{h}$ and $\hat{z}$ will not alter the scaled flow field variables.

(ii) Any isotropic horizontal stretching of the mountain shape will stretch the flow field accordingly without altering it otherwise. For example if $u(x, y, z)$ is known for the hill $h(x, y)$; then $u(sx, sy, z)$ is a solution for the hill $h(sx, sy)$ where s is an arbitrary stretching factor.

The existence of those scaling laws simplifies our task considerably. They reduce the number of numerical calculations required and provide a check on the numerics. The failure of the scaling laws provide an indication of the bifurcation, if the new state is not ideal.

2. Numerical calculations

2.1. Choice of a numerical model

Instead of devising a numerical scheme to solve eqs. (5–9, 11) directly, we turn to an existing operational time-dependent sigma-coordinate Limited Area Model (LAM) of the Norwegian Meteorological Institute (Grønås and Hellevik, 1982). The particular parameters used in the LAM runs are given in Table 1 and Appendix A. There are two primary differences between the LAM and our prototype problem (5–9, 11). First, the LAM is a fully time dependent model allowing the approach to steady-state and any later spontaneous time evolutions to be considered. A second and minor point is that the LAM includes compressibility effects while the Boussinesq equations do not. Compressibility effects are of order (L_z/H_s) where H_s is the density scale height. The value of this ratio is typically 0.05 to 0.2 for our runs and we have not been able to detect any compressibility effect on our results.

Table 1. *LAM deceleration runs*

Run	h (m)	L (km)	U_0 (m/s)	ε
27	1200	150	20 → 17	0.009
28	600	150	30 → 5	0.09
29	1000	150	25 → 10	0.015
30	400	150	12 → 6	0.06
31	500	150	12 → 6	0.04
32[1]	500	100	12 → 6	0.06
33	800	150	15 → 10	0.009
34[2]	50	150	15 → 7	0.012
35	800	300	15 → 10	0.018
36[3]	500	150	15 → 10	0.018
37[4]	800	150	15 → 11	0.009

Note that: $N_0 = 0.015$ for all runs and ε is computed at $\hat{h} = 1$. Unless otherwise stated, runs had no shear and a Gaussian hill. (1) Run 32 had a $\frac{3}{2}$ power hill. (2) Run 34 was used to study airstream deceleration. (3) Run 36 had forward shear. (4) Run 37 was a repeat of Run 33 with a long final period with $U = 11$. Steady state was not achieved.

One advantage of our sigma-coordinate model is its standard design. Other such models, with friction and rotation likewise removed, should be able to reproduce our results. Previous use of the model for mountain airflow research is reported by Sandnes (1987).

An axisymmetric Gaussian hill shape is used for these runs.

$$h(x, y) = h_0 e^{(x^2 + y^2)/L^2}. \tag{12}$$

This shape, while not having all the simplifying analytical properties of $\frac{3}{2}$ power hill used in Smith (1980), has the advantage of compactness. The Gaussian function decays rapidly with distance from the hill center. Some properties of (12) and a comparison with the $\frac{3}{2}$ power hill are given in Appendix B. An additional advantage of the Gaussian hill is that for this shape linear theory makes a clear prediction of stagnation below before stagnation aloft. The action of nonlinearity in reversing this prediction is therefore clearly seen.

In order to evaluate the accuracy of our LAM model we use three criteria: agreement with linear theory, agreement with the scaling laws and conservation of potential vorticity. To compare our LAM results with linear theory we performed a 48-h run to steady state with parameters: $\rho_0 = 1.24$ kg/m^3, $h_0 = 200$ m, $a = 150$ km, $U_0 = 15$ m/s, $N_0 = 0.015$ s^{-1} so that $\hat{h} = 0.2$. The LAM gave a drag $D = 1.45 \cdot 10^9$ Nt while linear theory (B.17) gives $D = 1.65 \cdot 10^9$ Nt. These values differ by 14%, probably because of the coarseness of our sigma level spacing.

The agreement of the computed wavefield with linear theory during the deceleration runs is shown on the left-hand side of Fig. 1 for $\hat{h} < 0.4$. The LAM predictions of perturbation speed agree to $\pm 10\%$ with linear theory when the time lag effect discussed in Appendix C is included. The other two criteria for evaluating the accuracy of the LAM are discussed in the later sections.

2.2. Deceleration strategy

One difficulty in analyzing nonlinearity and bifurcation is the problem of path dependence.

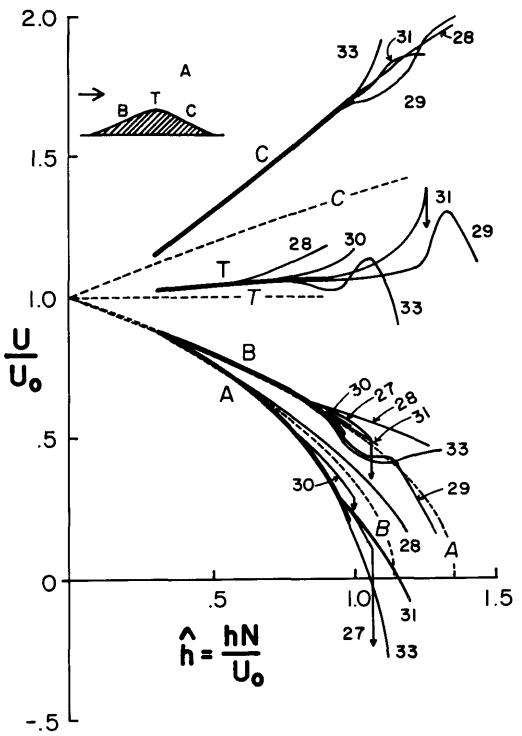

Fig. 1. Scaled speeds at four diagnostic points in the mountain wave field as functions of $\hat{h}$ for 6 deceleration runs. Collapsed curves (i.e., thick lines) are universal curves for unsheared flow over an axisymmetric Gaussian hill. Predictions of linear theory are shown dashed.

In a non-linear system such as eqs. (1–4), it is possible that a transition may appear at a different point and seem to have a different nature when approached from different directions in parameter space. For the sake of definiteness and reproducibility, we have used a deceleration strategy. A steady state flow is achieved in the model with a low value of $\hat{h}$ and then U_0 is slowly decreased giving a progressive increase in $\hat{h}$. Other investigators have also used this approach (e.g., Clark and Peltier, 1977; Crook et al., 1990). An advantage of the deceleration strategy is that it gives unlimited resolution along the parameter line $\hat{h}$. The response of the flow to deceleration at the inflow boundary is described in Appendix C.

The reader should be aware that the deceleration strategy does not illustrate all of the aspects of flow non-linearity or flow transition. The "start-up" strategy of SR89 and Rotunno and Smolarkiewicz (1991) gives a complementary view of these effects.

A non-dimensional measure of the deceleration rate in our runs is $\varepsilon \equiv U_t L/U^2$ which is the relative rate of decrease in speed (U_t/U) in a characteristic time ($\tau = L/U$). For sufficiently small ε, the flow should evolve through a sequence of steady states (if they exist) each characterized by $\hat{h}$. If a bifurcation point exists at $\hat{h} = \hat{h}_{crit}$ then the limit $\varepsilon \to 0$ will be discontinuous there. Beyond $\hat{h}_{crit}$ the flow will enter the time domain. As the flow evolves, the sequence of flow states will not obey the steady state scaling. We will attempt numerically to exhibit the properties of the $\varepsilon \to 0$ limit.

Seven LAM decelerations were performed with a variety of choices of dimensional parameters. By examining these in order of decreasing ε we get a sense of whether the $\varepsilon \to 0$ limit is being approached (i.e., runs 28, 30, 31, 35, 29, 27, 33). Examining them in order of dimensional mountain height (i.e., runs 30, 31, 28, 33, 35, 29, 27) gives an impression that the scaling law (i) is met in the prebifurcation state. Comparing 33 and 35 tests scaling law (ii).

2.3. *Universal curves*

The results from seven deceleration runs are plotted in Fig. 1. The speed at four points on the centerline of the flow field are used as diagnostic quantities.

A ... point of minimum windspeed above the lee slope

B ... point of minimum windspeed on the windward slope

C ... point of maximum windspeed on the lee slope

T ... point on the mountain top

Except for T, these points are defined as extrema in the wind field and as such, change their positions slightly with the control parameter.

With the exception of the two fastest deceleration runs (28 and 30) the diagnostic speed curves collapse to a single line for $\hat{h} \leqslant 1$ when scaled according to Section 1. This suggests that during the slow deceleration (i.e., $\varepsilon < 0.04$), the flows are nearly in steady state. The four curves (A, B, C, and T) are universal curves for the axisymmetric Gaussian hill shape in the sense that they apply to

any combination of ρ_0, N_0, U_0, h_0 and L. Empirical expressions for the universal curves can be derived as follows.

Following Smith (1990), the Bernoulli and hydrostatic equations can be combined to give

$$U^2 = U_0^2 - 2\frac{P^*}{\rho_0} - N_0^2\eta^2, \tag{13}$$

where P^* is the perturbation pressure. Eq. (13) can be rewritten as

$$U^2 = U_0^2 - 2N_0^2 I_\eta \tag{14}$$

where

$$I_\eta \equiv \int_0^\infty \eta \, \mathrm{d}\hat{z}_0 \tag{15}$$

is related to the perturbation pressure. The value of I_η at each of the four diagnostic points can be represented approximately by a two-term formula in $\hat{h}$

$$I_\eta = h\left(\frac{U_0}{N_0}\right)(\alpha + \beta\hat{h}). \tag{16}$$

Substituting (16) into (14) gives

$$\frac{U}{U_0} = (1 - 2(\alpha\hat{h} + \beta\hat{h}^2))^{1/2}. \tag{17}$$

The first coefficient α is derivable from linear theory in isosteric coordinates using an FFT solution for point A and analytical formulae derived in Appendix B for points B, C and T. The second coefficient β is determined from (16) using the LAM results at $\hat{h} = 0.9$. The results given in Table 2 provide a satisfactory fit to the universal curves from $\hat{h} = 0$ to 1.

2.4. *Comparison with linear theory*

Fig. 1, Table 2 and (17) facilitate a discussion of the non-linear effects in the prototype problem.

Table 2. *Universal curve coefficients for a Gaussian hill with no shear*

Point	α	β
A	0.368	0.12
B	0.439	−0.09
C	−0.439	−0.5
T	0.0	−0.05

The largest value of β in Table 2 is for point C indicating that of the four diagnostic points, C experiences the largest non-linear effect. The maximum lee side wind is substantially larger than predicted by linear theory. As we have used the exact diagnostic eq. (14), it may also be said that the magnitude of the lee side pressure perturbation and the integrated value of downward displacement (I_η) above the lee slope are underpredicted by linear theory.

At point B on the windward slope, the speed is greater than predicted by the linear theory, i.e., linear theory overpredicts the magnitude of the perturbation there. The fact that curve B lies close to the linear theory prediction for curve A is fortuitous.

Curve A, describing the speed in the wave breaking region aloft, is of particular interest. The LAM results shows a much stronger deceleration there than predicted by linear theory. The speed at point A approaches zero at about $\hat{h} = 1.1$, whereas linear theory (i.e., setting $\beta = 0$ in (17)) would give an $\hat{h}_{\mathrm{crit}} = 1.34$.

Probably the most surprising aspect of the universal curves is the relationship between curves A and B. Linear theory predicts that stagnation will first occur in the windward slope (point B) when in fact the opposite is true. Non-linear effects suppress stagnation at B while aiding stagnation at A.

Another difference from linear theory could be mentioned; the particle deceleration following the leeward wind maximum. According to linear theory, the speed of the accelerated leeside flow returns smoothly and monotonically to normal (i.e., U_0) downstream. According to our numerical results, for $\hat{h} \geqslant 0.9$, the wind four to five half-widths downstream on the surface is actually less than the freestream value. This, together with the effect of non-linearity on increasing the leeside wind maximum, implies a much greater particle deceleration rate and speed convergence over the lee slope. The vertical motion implied by this speed convergence may be associated with the non-linear enhancement of wave breaking aloft. It is probably not correct to consider this downwind speed minimum to be a precursor of the wake, as we will see in Subsection 2.6.

Curve T describes the windspeed at the hill top. According to linear theory for axi-symmetric hills, the perturbation wind speed should be zero at the

hill top. Fig. 1 shows that in fact there is a slight positive anomaly there. This is reflected in the small negative value for β.

2.5. *Discussion of stagnation and Sheppard's rule*

It was suggested by Sheppard (1956) that P^* in (13) might reasonably be neglected giving

$$U^2 = U_0^2 - N_0^2 \eta^2. \tag{18}$$

According to (18) air parcels climbing a mountain slope will slow, reaching a minimum speed at the mountain top where $\eta = h$. For a mountain equal to or higher than $h = U_0/N_0$, a stagnation point would form and the air would flow around rather than over the hill.

The Sheppard rule has been widely used (Hunt and Snyder, 1980; Gill, 1982, pages 293–294; Spangler, 1987) but has been criticized by one of the present authors (Smith, 1990) on the grounds that speed variations in stratified flows are primarily controlled by pressure variations in (13) rather than by vertical displacement. The dominance of the pressure effect over the lifting effect has been verified by SR89.

The results in Fig. 1 and 2 allow a further discussion of this point. Consider the speed at the mountain top (curve T in Fig. 1). Instead of finding the slowest flow at this point, as predicted by Sheppards rule, the speed here is slightly greater than the upstream speed. Clearly the conversion of kinetic energy to potential energy implied by (18), cannot be the dominant effects controlling the flow speed. The hill top air parcels are both higher and faster than they were upstream.

Consider the speed on the windward slope of the hill (point B). The local minimum in wind speed in this region is not because of the height of lifting. The lifting is even greater at the hill top where the speed is greater. Instead, it is the arching up of isentropes above this region which results in high pressure (through the hydrostatic law) and correspondingly low wind speed (through Bernoulli's Law).

Finally, consider the situation in the region of minimum speed above the lee slope (point A). It was proven by Smith (1990) that: In the interior of a steady state hydrostatic wave field, the wind speed extrema (maxima or minima) occur at points of zero vertical displacement. This statement, which is easily derived from (15), is the antithesis of Sheppard's rule (18). In Fig. 2, we see indeed that the point of minimum speed (A), occurs at a point in which the local isentropic surface is at the same elevation as it had upstream.

2.6. *Vertical and isentropic vorticity*

As a stagnation point forms at point A in the flow, one might expect the shear on either side of point A to contain vorticity, at least shear vorticity. The fact that vorticity is not necessarily present in such a situation is illustrated by stagnation points in classical potential flow around a

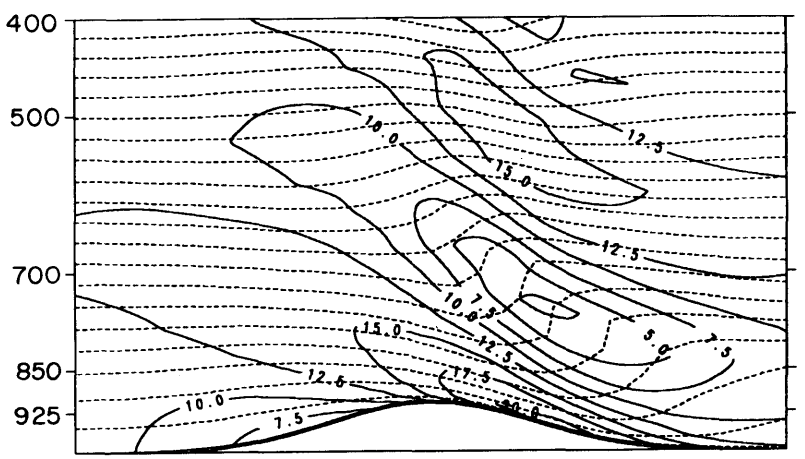

Fig. 2. Vertical cross-section of the flow before bifurcation in run 37 (time = 138 h). Solid lines are isotachs and the dashed lines are isentropes. Units on the vertical axis are hectopascals. The flow is from left to right.

Tellus A/45/1-3

cylinder in which shear and curvature vorticity exactly cancel. Vorticity patterns near point A on a theta surface and on a sigma surface are shown in Figs. 3, 4.

The existence of vorticity in mountain wave flow is of interest for two reasons. First, the presence of a vorticity component perpendicular to an isentropic surface

$$\zeta_\theta = (v_x - u_y)_\theta \tag{19}$$

would indicate that the conservation of potential vorticity and isentropic circulation are being violated by the numerical model. According to Fig. 3, there is a rather small amount of such vorticity. This is probably a residual arising from interpolation errors in the vicinity of the stagnation point where the theta surfaces are steeply tilted. The magnitude of the residual isentropic vorticity ($\approx 2 \cdot 10^{-5}\,s^{-1}$) can be understood by noting that the wind field is much more poorly resolved on an isentropic surface than it is on a sigma surface. This difference is evident near the stagnation point in Figs. 3, 4. Thus, truncation errors significantly influence our computation of isentropic vorticity. It is also possible that the non-zero residual isentropic vorticity reflects errors in the sigma-coordinate solution.

In spite of this problem, our results indicate a tendency to conserve vorticity on isentropic surfaces even though the numerical calculations were performed on sigma-surfaces. This result builds confidence in the Limited Area Model used in this study, while pointing out the need for higher resolution (as in SR89).

The striking difference between the vorticity patterns in sigma and theta surfaces allows us to discuss a more subjective issue; the existence of lee eddies when $\hat{h} < \hat{h}_{crit}$. In the present context, the issue of whether lee eddies are present in the subcritical mountain wave flow bears on the question of whether a bifurcation exists. If subcritical lee eddies exist, it would suggest that the transition in flow type at $\hat{h} = \hat{h}_{crit}$ is more gradual and the term "bifurcation" would be less appropriate.

For the present purpose, we define the term

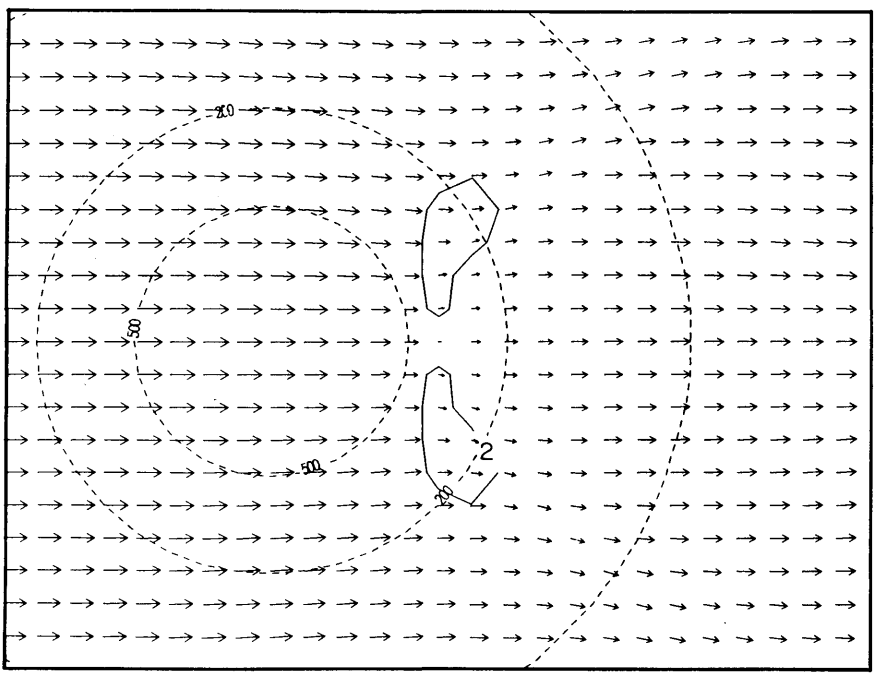

Fig. 3. Horizontal map on a isentropic surface ($\theta = 295$) cutting through the minimum wind point (A). The wind speed is shown with vectors and the vorticity (in units of $10^{-5}\,s^{-1}$) is contoured. The 100, 200 and 500 meter hill contours are shown dashed. The total hill height is 800 meters. As in Fig. 2, this diagram is from run 37 at time = 138 h.

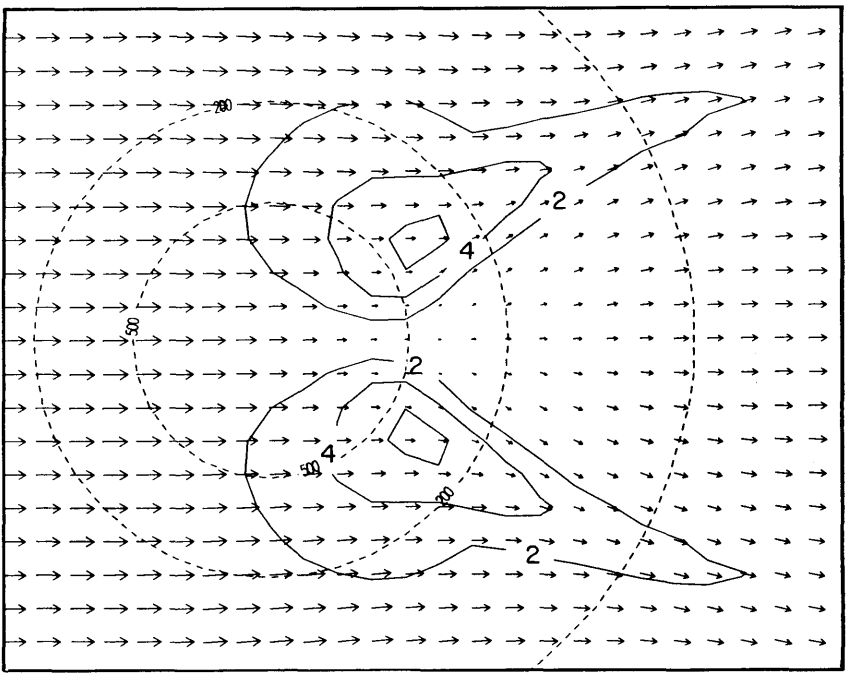

Fig. 4. Same as Fig. 3 but on a sigma surface number 11.

"eddy" to denote a region with vorticity (or circulation) of a type that is materially conserved or nearly so. With this definition, eddies are composed of an "advectable" quantity and this property gives an eddy many of its observed behaviours. The vorticity in common wake eddies, for example, drifts downstream under the influence of advection by the mean flow or, by mutual advection, two counter rotating wake eddies may manage to stay attached to a cylinder. In either case, the behaviour of the wake eddies involves the advectable nature of the vorticity within them. By the above definition of "eddy", fluid parcels cannot move freely through an eddy. In stratified flow, the materially conserved vorticity to be used in such arguments is the potential vorticity or equivalently, the isentropic circulation. Vertical vorticity would be excluded from this definition as it lacks a material conservation property.

In Fig. 4, the vortical regions have a fundamentally different nature than common eddies as no materially conserved quantity (such as potential vorticity) is involved. These are not "eddies" according to the definition above. They cannot advect each other or be advected by the mean flow as they are not composed of an "advectable" quantity. They do not have closed streamlines. Fluid parcels pass freely through them. They are, as shown by SR89, locally tilted vortex lines generated by baroclinic (or solenoidal) torques within the gravity wave field. The regions of vertical vorticity in Fig. 4 are stationary, not because of mutual advection, but because the stationary mountain waves, of which they are a part, are propagating upstream at a speed equal and opposite to the ambient flow.

It follows from the above definition that there are no "eddies" in subcritical mountain wave flow. After the bifurcation on the other hand, dissipation in breaking mountain waves can generate potential vorticity and "real" eddies can be formed. These real eddies could either remain fixed over the lee of the hill by mutual advection or drift downstream to form an extended wake. The reader can find a further discussion of this issue in the comment and reply by Smith (1989c), Smolarkiewicz and Rotunno (1989b) and Crook et al. (1990).

3. Comparison with Olympic Mountain observations

To see if the non-linear mountain wave effects described in Subsections 2.3 and 2.4 are observable in the atmosphere, we use the recent analysis of pressure fields around the Olympic Mountains by Mass and Ferber (1990). The Olympic Mountains satisfy the assumptions of the present paper about as well as any real mountain could. The total width of the mountain is about 70 km giving it a high Rossby number and making the flow hydrostatic. The mountain is roughly axisymmetric and has a height (1500 m) such that in the variable mid-latitude winds, the non-dimensional mountain height $\hat{h}$ swings through a range of values of interest for studying mountain airflow non-linearity. The observation of Mass and Ferber, of maximum and minimum perturbation pressure near the Olympic Mountain, is directly compatible with the universal curves for points B and C. Mass and Ferber define a perturbation pressure index.

$$\mathrm{PI} = P_C - P_B \tag{20}$$

indicating the pressure difference across the mountain and an asymmetry index

$$\mathrm{AI} = P_C + P_B \tag{21}$$

indicating the amount by which lee-side low is stronger than the windward side high. The observed pressure index is related to the incoming wind speed by their regression equation

$$\mathrm{PI} = 0.652 + 0.154U \tag{22}$$

while the asymmetry index has no evident correlation with wind velocity. Values of AI scatter about a mean value of

$$\mathrm{AI} = -0.7 \tag{23}$$

both expressed in hectopascals.

From (13, 15, 16) and Table 2,

$$\mathrm{PI} = \rho_0 hNU\left(0.878 + 0.41\frac{hN}{U}\right), \tag{24}$$

and

$$\mathrm{AI} = \rho_0 hNU(-0.59)\frac{hN}{U}, \tag{25}$$

$$= \rho_0 h^2 N^2(-0.59). \tag{26}$$

These formulae (24, 26) can be compared with (22, 23) by choosing $N = 0.01\ \mathrm{s}^{-1}$ and $h = 1500$ m, so that (24, 26) become

$$\mathrm{PI} = 1.1 + 0.16U, \tag{27}$$

$$\mathrm{AI} = -1.6, \tag{28}$$

expressed in hectopascals. The agreement between (22) and (27) is very good with respect to the linear term. The term arising from the nonlinearity in (27), i.e., 1.1, has the right sign but disagrees by a factor of two with constant term in (22). The constant terms in (23) and (28) also disagree by a factor of two, but have the same sign.

We conclude that the "universal" curves agree fairly well with the magnitude of the pressure difference across the Olympics and with the observation that the lee side low is more pronounced than the windward side high. We attribute the disagreement to factors such as stability and windspeed variations with height, latent heat release, and the non-axisymmetry of the Olympic Mountains. Also, some of the data which contributed to the regression curves (22, 23) corresponded to conditions with $\hat{h} > 1$, and therefore should not be compared with (27, 28).

4. The effect of shear

According to linear theory (i.e., Smith, 1989a), the presence of forward shear in the upstream wind profile can delay wave breaking and possibly allow stagnation on the windward slope to occur first. To check this possibility, run 33 was repeated with a shear corresponding to a Richardson number

$$\mathrm{Ri} = N_0^2/U_z^2 = 20, \tag{29}$$

and a value of $\varepsilon = 0.06$. The result of this run is shown in Fig. 5.

At $\hat{h} = 1$, U_B and U_C are similar to the unsheared case but U_A is much larger. As $\hat{h}$ is increased, U_B decreases smoothly to zero at about $\hat{h} = 1.6 \pm 0.1$. At this parameter setting, U_A is still large; about 90% of the reference flow speed at the ground (U_0).

We conclude that the effect of forward shear significantly changes the nature of the onset of stagnation. The critical value of $\hat{h}$ (based on the ground level wind) increases from 1.1 to 1.65 (for

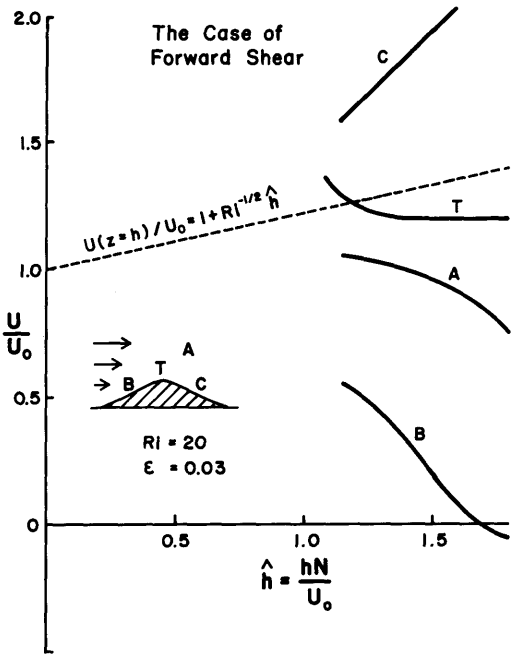

Fig. 5. Same as Fig. 1 but for the case with forward shear. The Richardson number is 20. The dashed line indicates the scaled freestream wind speed at an altitude equal to the height of the hill.

Ri = 20). Stagnation begins on the windward slope (point B) instead of in the wave breaking region aloft (point A).

5. Bifurcation and evolution in the time domain

When $\hat{h}$ exceeds unity, the curves in Fig. 1 begin to diverge. Further decrease in ε doesn't seem to help. This breakdown in the scaling laws suggests that a bifurcation has been reached and that the flow is evolving in the time domain. To check this idea, the deceleration of the inflow wind speed was halted near the end of three runs (27, 30 and 31). With $\hat{h}$ held fixed at values just exceeding unity, the flow continued to evolve as shown with the arrows in Fig. 1.

The existance of a bifurcation in 3-D mountain airflow would be very significant. Unfortunately, we are not in a good position to analyse the time evolution of the system or the nature of other steady states. There are two reasons for this. First, for unsteady flow, possibly with wave breaking, we do not have any scaling laws to assist in collapsing runs with different parameters onto universal curves. Second, our numerical model is hydrostatic, rather coarsely gridded, and its turbulence parameterization scheme (a Shapiro filter applied every 8 time steps) is not a physically based one. These model characteristics could result in an improper treatment of a flow with wavebreaking. Furthermore, we haven't successfully completed a numerical run in which a decelerated flow has slightly crossed the bifurcation boundary and then evolved to a new steady state.

It is useful however to consider a few possibilities for the nature of the flow fields for $\hat{h} > \hat{h}_{\text{crit}}$. Possibly: (i) no quasi-steady state exists or, (ii) the new steady state has continuous wave breaking near point A but with little other difference or, (iii) the new steady state adjusts itself to generate a stagnation point on the windward slope (point B). Option (iii) is particularly interesting to imagine. It says that stagnation at point B is not approached progressively as $\hat{h}$ increases. Instead, stagnation occurs at point A first, aided by flow nonlinearity, and this triggers evolution in the time domain leading to stagnation at point B.

One further run was completed to test Option (iii). In Run 37, Run 33 was repeated, ending with a long period with constant wind speed and $\hat{h} = 1.2$. Steady state was not achieved however. The properties in the wake region fluctuated slowly in time. The value of $\hat{h} = 1.2$ exceeds the critical value by so little that if the universal B curve is extended, (see Fig. 1) one would not predict stagnation at point B. As shown in Fig. 6 however, the flow is nearly stagnated at B and a turbulent non-ideal wake exists as well. This result should be tested with other types of numerical models.

Option (iii) would be consistent with other lines of evidence. Laboratory experiments (Hunt and Snyder, 1980) suggest that the critical mountain height for low level flow blocking is $\hat{h} \approx 1$ where our extrapolated universal curves for point B indicate a significantly higher value. Low level stagnation induced by wave breaking would explain this discrepancy.

The Option (iii) interpretation of the bifurcation is also supported by the recent work of Crook et al. (1990, henceforth CCM90). CCM90 did numerical deceleration experiments, similar to

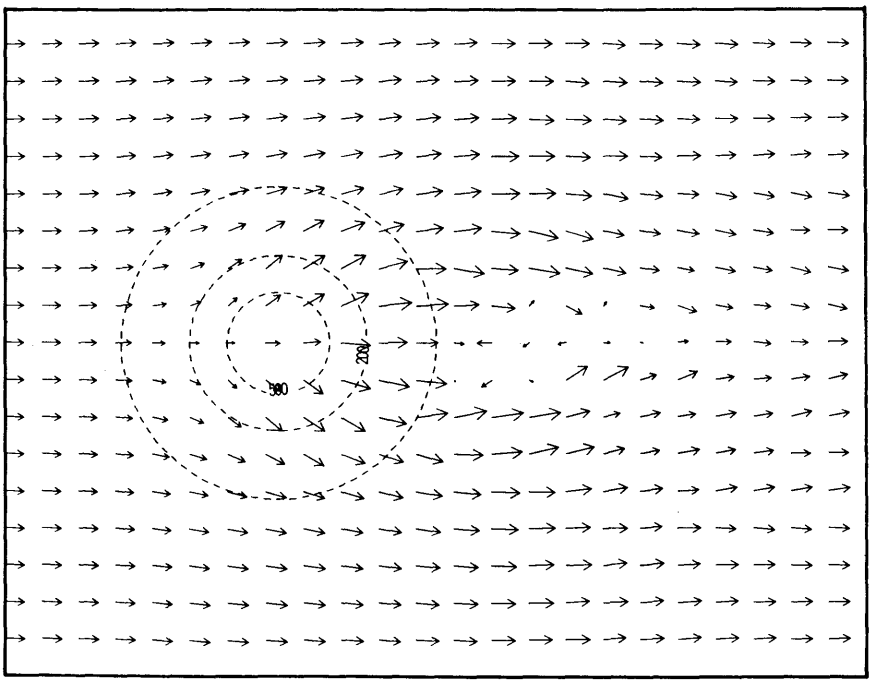

Fig. 6. Horizontal map on the lower boundary showing the wind (vectors) and topography (dashed) at the end of Run 37. This pattern is not in steady state, even though the wind speed has been held constant for 100 h. The parameter $\hat{h} = 1.2$.

those described here, but with a non-hydrostatic model and with a first-order-closure turbulence parameterization scheme. As their upstream flow was decreased and the value of $\hat{h}$ climbed above the critical value "the wave first breaks aloft and then the region of flow reversal descends to the ground." This description from CCM90 agrees with our interpretation of wave breaking triggering a bifurcation which leads to stagnation below.

One limitation on the CCM90 study is the rapid rate of deceleration used in their model experiments. Their value of $\varepsilon = 0.4$ is about an order of magnitude larger than the small value found herein to be necessary to approach steady state (i.e., $\varepsilon = 0.04$). Thus, during their deceleration runs, a changing sequence of steady state flows would be indistinguishable from evolution in the time domain. Evidence of a bifurcation would be obscured.

If Option (iii) is correct, it provides an interesting contrast to the bifurcation in 2-D flow (Clark and Peltier, 1977). In 2-D, wave breaking leads to severe downslope winds while in 3-D it leads to stagnation on the windward slope and reverse flow in the wake.

The global consequence of 3-D mountain airflow bifurcation is difficult to judge. The Earth's rough surface includes a range of terrain heights which span the typical characteristic height $L_z = U/N$ in the Earth's atmosphere. Thus, as the winds rise and fall at locations around the globe, the local non-dimensional mountain heights fluctuate about the critical value and mountain airflow patterns are frequently in a state of transition from one type of steady state to another. This transition from "wave to wake" flow and back again occurs on a time scale which is unconnected to the time-scale on which the incident wind might be changing. Even slowly varying global wind patterns would generate "switching" or "bifurcation" noise from hilly terrain. It would be interesting to know how this effect compares with flow instabilities (e.g., convective, barotropic, and baroclinic) as a source of chaos in the Earth's atmosphere.

6. Conclusions

We have shown that the scaling laws for ideal hydrostatic non-rotating flow can be demonstrated in a simple sigma-coordinate model. According to these laws, the nature of the flow depends only on the non-dimensional mountain height and not on mountain width or slope. When the upstream flow is decelerated, steady state conditions are approximated when $\varepsilon = U_t L^2/U \leqslant 0.04$.

There are considerable non-linear effects in the parameter range $0.3 < \hat{h} < 1.0$. As $\hat{h}$ approaches unity, non-linearity enhances stagnation aloft and lee slope acceleration while reducing the tendency for stagnation on the windward slope. The universal curves describing the approach to stagnation agree qualitatively with pressure observations from the Olympic Mountains (Mass and Ferber, 1990).

For the axisymmetric Gaussian hill, a stagnation point forms aloft when the value of non-dimensional hill height is $\hat{h} = 1.1 \pm 0.1$. For the $\frac{3}{2}$-power hill, the critical value is slightly higher, $\hat{h} = 1.2 \pm 0.2$. These values are significantly larger than the corresponding values for an infinite ridge ($\hat{h}_{crit} = 0.85$ for a Witch-of-Agnesi ridge, Huppert and Miles, 1969).

There is a bifurcation near $\hat{h} = \hat{h}_{crit}$, where the ideal scaling laws break down and evolution in the time domain begins. The bifurcation correlates well with the onset of stagnation in the wave field on the centerline above the hill. Although the term "wave breaking" is probably appropriate, we offer no detailed conceptual model for the cause of the bifurcation.

During deceleration of the ambient flow, the onset of windward slope stagnation and flow splitting does not occur progressively as $\hat{h}$ increases but rather occurs in the time domain following the bifurcation. There is no steady state pre-bifurcation solution with the speed on the lower boundary less than half the freestream speed.

The use of Sheppard's rule to understand flow stagnation is shown to be incorrect. As the non-dimensional hill height increases, the minimum flow speed does not occur at points of large vertical displacement as predicted by Sheppard's rule. In fact the opposite is true. The minimum speed in the flow is at a point where the vertical displacement of fluid particles is zero.

The nature of the 3-D bifurcation and the onset of flow splitting is fundamentally changed by forward shear in the environment due to the suppression of wave breaking. Even with a relatively small forward shear (e.g., Ri = 20), stagnation occurs first on the windward slope ($\hat{h}_{crit} = 1.6 \pm 0.1$).

The (unsheared) 3-D mountain airflow bifurcation is similar to the bifurcation in 2-D in that it is triggered by stagnation aloft; but it also different. The third dimension allows flow splitting and wake formation in ways that are not topologically possible in two dimensions. The 3-D bifurcation causes a drop, or even a reversal, rather than a rise in leeside wind speed (SR89).

7. Acknowledgements

Conversations with C. Schär, P. Smolarkiewicz, R. Rotunno, P. Baines, S. Thorsteinsson, A. Crook, Y.-L. Lin, and A. Bratseth are appreciated. Anstein Foss and Paul Gluhosky assisted with the calculations and plotting. This work was partly supported by the National Science Foundation, Division of Atmospheric Science, grant ATM-8914138 and the Royal Norwegian Council for Scientific and Industrial Research IT2.28.2193.

Appendix A
The DNMI numerical model

The Limited Area Model (LAM) of the Norwegian Meteorological Institute (DNMI) is a sigma-coordinate model with staggered grid as described by Grønås and Hellevik (1984). Errors in the horizontal pressure gradient are reduced using the method of Janjic (1977). For the present purposes, all physics and boundary layer parameterizations are removed from the model. The model is run with a $120 \times 120 \times 120$ grid. The horizontal grid spacing is uniform at 25 km while the twenty sigma levels are distributed unevenly in the vertical. Sigma is defined

$$\sigma = \frac{p - p_{top}}{p_{surface} - p_{top}}, \tag{A.1}$$

with $p_{top} = 100$ hPa.

The distribution of levels is given in Table 3.

In Table 3, $p^{(1)}$ is pressure at each level if

Table 3. *Sigma levels in the LAM*

Level	σ	$p^{(1)}$ (hPa)	$z^{(2)}$ (km)
1	0.050	145.0	16.4
2	0.135	221.5	12.8
3	0.205	284.5	10.7
4	0.275	347.5	8.98
5	0.345	410.5	7.57
6	0.415	473.5	6.35
7	0.485	536.5	5.29
8	0.555	599.5	4.35
9	0.625	662.5	3.5
10	0.695	725.5	2.73
11	0.765	788.5	2.02
12	0.820	838.0	1.5
13	0.860	874.0	1.14
14	0.890	901.0	0.89
15	0.910	919.0	0.72
16	0.930	937.0	0.55
17	0.950	955.0	0.39
18	0.970	973.0	0.23
19	0.985	986.5	0.16
20	0.995	995.5	0.04

$p_{\text{surface}} = 1000$ hPa and $z^{(2)}$ is the approximate altitude above the 1000 hPa surface ($z = H_s \ln(p_s/p)$). The vertical spacing varies from 120 m near the ground to 3600 meters at the top of the domain. The expected vertical length scale for the flow $L_z = U_0/N_0$ varies from 400 m for $U_0 =$ 6 m/s to 1000 m for $U_0 = 15$ m/s. Thus, the vertical structure of the flow is well resolved up to about 2 km in the former case; up to 6 km in the latter case. Our vertical resolution is not as fine as that achieved by some other investigators. SR89 for example, had 80 levels in the vertical.

To reduce reflection, a linear damping is applied to the uppermost 6 layers with a coefficient $\gamma = 0.005$ such that disturbances in these layers decay with a characteristic time $\tau_\gamma = \Delta/\gamma =$ 75 s/0.005 $\approx$ 4 h. The time it takes for wave energy to propagate through one vertical scale is given by $T = L_z/Cg_z$ where the vertical component of the group velocity $Cg_z \approx U_0^2/N_0 L \approx 0.15$ m/s for $U_0 =$ 15 m/s and $L = 150$ km. In this case $L_z = 1.5$ km, $T \approx 3$ h and thus the wave will decay appreciably as it propagates vertically towards the upper boundary.

The horizontal grid spacing of 25 km is significantly less than the mountain half width $L = 150$ km. One run with $L = 300$ km showed little difference. After the bifurcation, a scale collapse occurs and considerable grid point noise is generated. This noise is controlled with a spatial filter applied every 8 time steps. We have not achieved "large eddy convergence" as we have not demonstrated that the primary flow features are insensitive to our handling of the small scales. For this reason we put little weight on the details of the post-bifurcation flow fields.

Appendix B
The Gaussian hill

For the current analysis we have used an axisymmetric Gaussian hill:

$$h(x, y) = h_0 e^{-r^2/L^2}, \tag{B.1}$$

where $r \equiv (x^2 + y^2)^{1/2}$. The volume of the Gaussian hill is:

$$V = h_0 \int_0^{2\pi} \int_0^{\infty} e^{-r^2/L^2} r \, dr \, d\phi = h_0 \pi L^2. \tag{B.2}$$

The Fourier Transform of (B.1) is

$$\hat{h}(\kappa, \psi) = \frac{h_0}{4\pi^2} \int_0^{2\pi} \int_0^{\infty} e^{-r^2/L^2} \times e^{i\kappa r \cos(\phi - \psi)} r \, dr \, d\phi, \tag{B.3}$$

where polar coordinates are used: $(x, y) \to (r, \phi)$ and $(k, l) \to (\kappa, \psi)$. Note that in this appendix the symbol $\hat{h}$ is the Fourier transform of the dimensional mountain shape, not the non-dimensional mountain shape.

Using

$$\int_0^{2\pi} e^{b \cos \phi} \, d\phi = 2\pi J_0(ib), \tag{B.4}$$

eq. (B.3) takes the form of a Hankel Transform (Miles, 1971)

$$\hat{h}(\kappa) = \frac{h_0}{2\pi} \int_0^{\infty} e^{-r^2/L^2} J_0(\kappa r) \, r \, dr, \tag{B.5}$$

which gives

$$\hat{h}(\kappa) = \frac{h_0}{2\pi} \frac{L^2}{2} e^{-\kappa^2 L^2/4}. \tag{B.6}$$

Following Smith (1989a), the field of vertical displacement is

$$\eta(r, \phi, \hat{z}_0) = \int_0^{\infty} \int_0^{2\pi} \hat{h}(\kappa) \times e^{im\hat{z}_0} e^{i\kappa r \cos(\psi - \phi)} \kappa \, d\kappa \, d\psi, \quad \text{(B.7)}$$

where $m = N_0/U_0 \cos\psi$. Similar expressions for η_{xz} and I_η can be derived from (B.7) by including the factor $(-N_0\kappa/U_0)$ or $(iU_0 \cos\psi/N_0)$, respectively. As with the $\frac{3}{2}$ power hill, these integrals are difficult to evaluate analytically but take on a simpler form at $\hat{z}_0 = 0$. Eq. (B.7) reduces to

$$\eta(r, \phi, \hat{z}_0 = 0) = 2\pi \int_0^{\infty} \hat{h}(\kappa) J_0(\kappa r) \kappa \, d\kappa, \quad \text{(B.8)}$$

which reduces to (B.1), while

$$\eta_{xz}(r, \phi, \hat{z}_0 = 0) = 2\pi \frac{N_0}{U_0} \int_0^{\infty} \hat{h}(\kappa) \times J_0(\kappa r) \kappa^2 \, d\kappa, \quad \text{(B.9)}$$

$$\eta_{xz}(r, \phi, \hat{z}_0 = 0) = -\sqrt{\pi} \frac{h_0 N_0}{L U_0} \times M\left(\frac{3}{2}, 1, -\frac{r^2}{L^2}\right), \quad \text{(B.10)}$$

$$I_\eta(r, \phi, \hat{z}_0 = 0) = -2\pi \frac{U_0}{N_0} \cos\phi \int_0^{\infty} \hat{h}(\kappa) \times J_1(\kappa r) \kappa \, d\kappa, \quad \text{(B.11)}$$

$$I_\eta(r, \phi, \hat{z}_0 = 0) = -\frac{\sqrt{\pi}}{2} \frac{h_0 U_0 r}{N_0 L} \cos\phi \times M\left(\frac{3}{2}, 2, -\frac{r^2}{L^2}\right), \quad \text{(B.12)}$$

where $M(a, b, c)$ is the confluent hypergeometric function (Abramowitz and Stegun, p. 486).

For the purposes of Section 3, the maximum and minimum I_η and the total drag are required. The extrema of (B.12) are

$$\text{Max}(I_\eta) = -\text{Min}(I_\eta) = \left(h_0 \frac{U_0}{N_0}\right)(0.445) \quad \text{(B.13)}$$

at $y = 0$ and $r = x = \pm 0.85L$. The value 0.445 compares well with the 0.439 value (see Table 2) from the FFT method. We have no such check on the interior extrema of I_η.

The drag on the Gaussian hill can be found using the Convolution Theorem

$$D = \rho_0 N_0^2 \iint I_\eta \frac{\partial h}{\partial x} \, dx \, dy, \quad \text{(B.14)}$$

$$= \rho_0 N_0^2 4\pi^2 \iint \frac{k}{m} \hat{h}(k, l) \hat{h}^*(k, l) \, dk \, dl. \quad \text{(B.15)}$$

Using (B.6), (B.15) becomes

$$D = +\rho_0 N_0^2 (4\pi^2) \left(\frac{h_0}{2\pi}\right)^2 \left(\frac{L^2}{2}\right)^2 \times \int_0^{2\pi} \int_0^{\infty} e^{-\kappa^2 L^2/2} \frac{k}{m} \kappa \, d\kappa \, d\psi \quad \text{(B.16)}$$

$$= +C\rho_0 N_0 U_0 L h_0^2, \quad \text{(B.17)}$$

where $C = (2\pi)^{3/2}/16 = 0.9843$.

The linear theory prediction for the axisymmetric $\frac{3}{2}$ power and Gaussian hills can be compared as follows. For the $\frac{3}{2}$ power hill, stagnation is predicted to begin simultaneously at points A and B as the two critical mountain heights are equal; $\hat{h}_A = \hat{h}_B \approx 1.3$. For the Gaussian hill; $\hat{h}_A = 1.36$ and $\hat{h}_B = \frac{1}{2}(0.445) = 1.12$.

The actual non-linear occurrence of stagnation was investigated by repeating run 33 with a $\frac{3}{2}$ power hill. The unversal curves for the $\frac{3}{2}$ power hill are very similar the those for the Gaussian hill; the same tendency for stagnation aloft is seen. The critical mountain height for the $\frac{3}{2}$ power hill is about $\hat{h}_A = 1.2$; slightly higher than for the Gaussian hill.

Appendix C

The effect of deceleration

As we have chosen to investigate the mountain airflow bifurcation using a deceleration strategy, it is worthwhile to consider how the deceleration occurs in the model. The deceleration is accomplished by prescribing a decreasing wind with time at the inflow boundary. As the specified deceleration is the same at all levels, it is transmitted to the domain by means of the lowest mode gravity

acoustic wave in the model, i.e., the mode with no vertical structure.

We have examined this behavior by noting that during deceleration, the mean speed near the hill (1500 km from the inflow boundary) lags the inflow speed by about 3 h. This lag has been neglected in our data analysis. At the smallest ε used here, correcting for the lag would shift the universal curves downward by 3%.

The characteristic time for mountain airflow evolution is

$$T = L/U_0 \tag{C.1}$$

This represents the time for an air parcel to pass over the hill or alternatively, the time required for wave energy in hydrostatic gravity waves to propagate vertically a distance L_z. It could take about five characteristic time units for energy to reach the upper boundary. For $U_0 = 6$ m/s, $T \approx 7$ h, thus the domain adjusts to the changing inflow condition faster than does the mountain induced disturbance.

During the deceleration, each fluid particle in the computational domain experiences a horizontal pressure gradient proportional to the deceleration rate.

$$\rho \frac{\partial u}{\partial t} = -\frac{\partial p}{\partial x}, \tag{C.2}$$

which is nearly constant over the domain. This pressure gradient produces a force on the hill according to Archimedes Law

$$D = -\frac{\partial p}{\partial x} \cdot V, \tag{C.3}$$

where the volume V for the Gaussian hill is given by (B.2), (B.17), (C.2), (C.3). We can estimate the ratio R of the deceleration drag to the mountain wave drag, using

$$R = \frac{\text{decelerationdrag}}{\text{mtn. wavedrag}} = \frac{\pi}{C} \varepsilon \hat{h}^{-1}, \tag{C.4}$$

where $\pi/C \approx 3.3$.

If for example $\varepsilon = -0.01$, a small hill with $\hat{h} = 0.1$ would experience a thirty percent drop in total drag due to the deceleration effect. This decrease in the drag is evident in each of our runs as soon as the deceleration begins.

REFERENCES

Abramowitz, M. and Stegun, I. A. 1965. *Handbook of mathematical functions.* Dover Publications, New York, 1046 p.

Brighton, P. W. M. 1978. Strongly stratified flow past three-dimensional obstacles. *Quart. J. Roy. Met. Soc. 104*, 289–307.

Castro, I. P. 1987. A note on lee wave structures in stratified flow over three dimensional obstacles. *Tellus 39A*, 72–81.

Castro, I. P., Snyder, W. H. and Marsh, G. L. 1983. Stratified flow over three dimensional ridges. *J. Fluid Mech. 135*, 261–282.

Clark, T. L. and Peltier, W. R. 1977. On the evolution and stability of finite amplitude mountain waves. *J. Atmos. Sci. 34*, 1715–1730.

Crook, N. A., Clark, T. L. and Moncrieff, M. W. 1990. The Denver cyclone. Part I: Generation in low Froude number flow. *J. Atmos. Sci. 47*, 2725–2742.

Drazin, P. G. 1961. On the steady flow of a fluid of variable density past an obstacle. *Tellus 13*, 239–251.

Gill, A. E. 1982. *Atmosphere-ocean dynamics*, Academic Press, New York, 662 p.

Grønås, S. and Hellevik, O. E. 1982. *A limited area prediction model at the Norwegian Meteorological Institute.* Technical Report No. 61, The Norwegian Meteorological Institute, Oslo, Norway.

Huppert, H. E. and Miles, J. W. 1969. Lee waves in a stratified flow: Part 3. Semi-elliptical obstacles. *J. Fluid Mech. 35*, 481–496.

Hunt, J. C. R. and Snyder, W. H. 1980. Experiments on stably and neutrally stratified flow over a model three-dimensional hill. *J. Fluid Mech. 96*, 671–704.

Janjic, Z. 1977. Pressure gradient force and advection scheme used for forecasting with steep and small scale topography. *Beit. Phys. der Atmos. 50*, 186.

Long, R. R. 1955. Some aspects of the flow of stratified fluids. I Continuous density gradients. *Tellus 7*, 341–357.

Mass, C. F. and Ferber, G. K. 1990. Surface pressure perturbations produced by an isolated mesoscale topographic barrier. Part 1: General characteristics and dynamics. *Mon. Wea. Rev. 118*, 2579–2596.

Miles, J. W. 1971. *Integral transforms in applied mathematics.* Cambridge University Press, London, England, 97 p.

Rotunno, R. and Smolarkiewicz, P. K. 1991. Further results on lee vortices in low-Froude-number flow. *J. Atmos. Science 48*, 2204–2211.

Sandnes, H. 1987. Stromninger rundt og over mesoscala fjell. Ph.D. Thesis, University of Oslo, Oslo, Norway.

Sheppard, P. A. 1956. Airflow over mountains. *Quart. J. Roy. Met. Soc. 82*, 528.

Smith, R. B. 1980. Linear theory of stratified hydrostatic flow past an isolated mountain. *Tellus 32*, 348–364.

Smith, R. B. 1985. On severe downslope winds. *J. Atmos. Sci. 42*, 2597–2603.

Smith, R. B. 1989a. Mountain induced stagnation points in hydrostatic flow. *Tellus 41A*, 270–274.

Smith, R. B. 1989b. Hydrostatic airflow over mountains. *Advances in Geophysics 31*, 1–41.

Smith, R. B. 1989c. Comment on "Low Froude number flow past three dimensional obstacles. Part I: Baroclinically generated lee vortices" by P. K. Smolarkiewicz and R. Rotunno. *J. Atmos. Sci. 46*, 3611–3613.

Smith, R. B. 1990. Why can't stably stratified air rise over high ground? In: Atmospheric Processes over complex terrain, ed. W. Blumen. *Meteorological Monographs 23*, 105–107, American Meteorological Society, Boston.

Smolarkiewicz, P. K. and Rotunno, R. 1989a. Low Froude number flow past three dimensional obstacles. Part I: Baroclinically generated lee vortices. *J. Atmos. Sci. 46*, 1154–1164.

Smolarkiewicz, P. K. and Rotunno, R. 1989b. Reply Econcerning "Low Froude number flow past three dimensional obstacles. Part I: Baroclinically generated lee vortices" by P. K. Smolarkiewicz and R. Rotunno. *J. Atmos. Sci. 46*, 3614–3617.

Smolarkiewicz, P. K. and Rotunno, R. 1990. Low Froude number flow past three dimensional obstacles. Part II: Baroclinically generated lee vortices. *J. Atmos. Sci. 46*, 1154–1164.

Spangler, T. C. 1987. Comparison of actual dividing streamline height to height prediction using the Froude number. *J. Climate Appl. Meteor. 26*, 204–207.